energies

MDPI

Article

Analysis and Controller Design of a Universal Bidirectional DC-DC Converter

Kou-Bin Liu [1,†], Chen-Yao Liu [1,†], Yi-Hua Liu [2,*], Yuan-Chen Chien [1], Bao-Sheng Wang [1] and Yong-Seng Wong [1]

1 National Synchrotron Radiation Research Center, No. 101 Hsin-Ann Road, Hsinchu Science Park, Hsinchu 30077, Taiwan; kbl@nsrrc.org.tw (K.-B.L.); cyl@nsrrc.org.tw (C.-Y.L.); ycchien@nsrrc.org.tw (Y.-C.C.); wang.bs@nsrrc.org.tw (B.-S.W.); wong.ys@nsrrc.org.tw (Y.-S.W.)

2 Department of Electrical Engineering, National Taiwan University of Science and Technology, EE-105-1 #No.43, Sec. 4, Keelung Rd., Da'an Dist., Taipei 10600, Taiwan

* Correspondence: yhliu@mail.ntust.edu.tw; Tel.: +886-2-2733-3141 (ext. 1252); Fax: +886-2-2737-6699

† These authors contributed equally to this work.

Academic Editor: Ali M. Bazzi

Received: 29 April 2016; Accepted: 24 June 2016; Published: 29 June 2016

Abstract: In this paper, first the operating principles of a non-isolated universal bidirectional DC-DC converter are studied and analyzed. The presented power converter is capable of operating in all power transferring directions in buck/boost modes. Zero voltage switching can be achieved for all the power switches through proper modulation strategy design, therefore, the presented converter can achieve high efficiency. To further improve the efficiency, the relationship between the phase-shift angle and the overall system efficiency is analyzed in detail, an adaptive phase-shift (APS) control method which determines the phase-shift value between gating signals according to the load level is then proposed. As the modulation strategy is a software-based solution, there is no requirement for additional circuits, therefore, it can be implemented easily and instability and noise susceptibility problems can be reduced. To validate the correctness and the effectiveness of the proposed method, a 300 W prototyping circuit is implemented and tested. A low cost dsPIC33FJ16GS502 digital signal controller is adopted in this paper to realize the power flow control, DC-bus voltage regulation and APS control. According to the experimental results, a 12.2% efficiency improvement at light load and 4.0% efficiency improvement at half load can be achieved.

Keywords: bidirectional buck–boost DC-DC converter; zero voltage switching; adaptive phase-shift control

1. Introduction

The energy crisis has recently become an important issue. To solve this, the development of renewable energy is essential. However, renewable energy sources are susceptible to weather factors which result in unstable power supply and unpredictable power generation. Thus, energy storage devices such as batteries are often applied in renewable energy generation systems. On the other hand, with the growing concern about global warming, countries have begun to target reducing greenhouse gas emissions. For the purpose of environmental protection and fuel cost reduction, automobile manufacturers have put great efforts into developing electric vehicles (EVs). In the near future, EVs are expected to be the mainstream of the transportation sector [1–3]. In a renewable energy generation system, a bidirectional DC-DC converter is typically used to interface the energy storage device with the renewable energy sources. When the power demand is lower than that provided, the excessive energy will be stored in the batteries, which is called charging mode. Conversely, when the power demand is higher than that provided, the energy flows from batteries to the load,

which is called discharging mode. For charging modes, if the voltage of battery is higher than that of the DC link, the system will boost the voltage to charge; otherwise, the voltage will be lowered to charge. For discharging modes, if the voltage of battery is higher than that of the DC link, the voltage of batteries will be lowered to discharge; otherwise, the voltage of batteries will be boosted to discharge. For a bidirectional DC–DC converter of an EV, the operation modes are basically the same. In acceleration or cruising mode, the energy should be delivered from the battery to the DC link, whereas in regenerative mode, the energy should be delivered from the DC link to the battery. For both modes, the bidirectional DC-DC converter utilized should be capable of converting the DC-bus voltage into a wide range of battery operating voltages. When all these possibilities are considered, a universal bidirectional DC-DC converter capable of operating in all directions with voltage stepping-up and stepping-down capabilities is a necessity.

Various bidirectional DC-DC converters have been proposed in the literature [4–32]. Typically, they can be divided into isolated and non-isolated types, depending on their isolation requirements as well as the required voltage transfer ratio. Compared with isolated converters, non-isolated ones boast advantages such as fewer parts, lower cost and compactness. Therefore, the non-isolated bidirectional DC-DC converter will be the main focus of this study. For non-isolated bidirectional DC-DC converters, soft switching techniques are typically employed to achieve high efficiency. A common way to accomplish soft switching is to employ an auxiliary circuit including auxiliary switches, inductors and/or capacitors [6–9]. Using this method, zero voltage switching (ZVS) or zero current switching (ZCS) can be attained by resonance between inductors and capacitors. Nonetheless, these techniques require additional components, which will result in higher costs and complexity. Another approach to realize soft switching is to adopt coupled inductors [10–19]. By adding an additional winding, it can form another power flow path to achieve ZVS or ZCS. However, the efficiencies under light load conditions are typically low due to the fact that the recycled energy will increase when the load decreases for this type of system. The third technique is to use interleaved structures in which several bidirectional DC-DC converters are connected in parallel to constitute a multiphase system [20–24]. For interleaved configurations, the efficiency at light load can be raised by phase-shedding techniques and the effective ripple can be reduced by introducing a phase-shift between the gating signals. However, this type of system suffers the disadvantages of high part counts and high costs. Finally, novel modulation strategy and/or novel topologies can be utilized to obtain high efficiency operation. In [25,26], simple structures and simple control strategy is proposed. These circuits suffer the disadvantage of low efficiency under heavy load condition due to hard-switching. In [27], sliding mode control is proposed to improve the performance of bidirectional DC-DC converters, the soft switching issue is not addressed since the proposed system utilizes conventional cascade buck/boost structure. In [28], a novel ZVS control technique based on discontinuous conduction mode is proposed. The presented control approach can achieve reliable ZVS within the entire operating range without additional circuits. However, the proposed system cannot realize universal bidirectional operations. In fact, all the aforementioned techniques can only be operated in buck mode for one direction and in boost mode for the other direction, and they cannot be operated vice versa. Therefore, developing a universal bidirectional DC-DC converter which is capable of operating in all directions with voltage stepping-up and stepping-down capabilities becomes essential. Dual-active bridge DC-DC converters can provide universal bidirectional power conversion; however, these topologies require a large number of power switches (typically eight). Moreover, they are all isolated type bidirectional DC-DC converters [29]. In [30,31], a novel low loss modulation strategy with simple circuit configuration is proposed. The advantages of these systems include high efficiency, no additional cost and a simple structure. Although the converter proposed in [30] can achieve universal bidirectional power conversion, details on how to realize universal bidirectional operation is not provided in [30]. Moreover, the phase shift value utilized in these papers is fixed, which may deteriorize the efficiency. Another nonisolated type bidirectional DC-DC converter which

is able to attain universal bidirectional power conversion is proposed in [32]. However, soft switching is not realized in this work.

This paper focuses on improving the efficiency of the bidirectional DC-DC converters proposed in [30]. First, the control signal requirements will be analyzed and extended to universal bidirectional operations (i.e., the capability of operating in all power transferring directions in both buck/boost modes). The implemented universal bidirectional DC-DC converter is applicable to renewable energy generation systems and EVs and can be placed between the energy storage device and the DC-bus regardless of the nominal voltage ratings of the battery and the DC link. With proper design of the control signal and the buck-boost inductance, ZVS can be successfully achieved and thus high efficiency can be obtained. To further improve the efficiency, an adaptive phase-shift (APS) control method which determines the phase-shift value between gating signals according to the load level is also proposed. Various efficiency enhanacement techniques regarding adaptive or variable phase-shift control have been proposed in the literature [33–35]. In [33], changing modulation method according to load conditions has been suggested, pulse-width modulation (PWM) are utilized to replace phase-shift control under light-load condition to reduce the circulating loss of phase-shift full-bridge converter. In [34,35], new control methods for full-bridge LLC resonant converters are presented. Fxed-frequency phase-shifted pulse width modulation and phase-shifted gate signals based on predetermined optimal duty ratio are used to regulate the output voltage at light load in [34,35], respectively. However, these approaches mainly focus on the improvement of light-load efficiency only. In addition, these techniques are all multi-mode control methods; hence, the control parameters are not tuned on-line. In this paper, the power flow control, dc-bus voltage regulation and APS control are implemented using a low cost dsPIC33FJ16GS502 digital signal controller. As the modulation strategy is a software-based solution, no additional circuits are required, therefore, it can be implemented easily with reduced instability and noise susceptibility problems. To validate the correctness and the effectiveness of the proposed method, a 300 W prototyping circuit is implemented and tested. As can be seen from the experimental results, the proposed converter is capable of operating in all power conditions correctly and high efficiency can be obtained. Compared to traditional fixed phase-shift method, the proposed APS control method can enhance both light-load efficiency and half-load efficiency by 10.1%–13.6% and 3.0%–4.8%, respectively.

2. Operating Principle of the Universal Bidirectional DC-DC Converter

The proposed universal bidirectional DC-DC converter is composed of an inductor, two capacitors and four power switches, as shown in Figure 1 [29]. By comparing the battery voltage (V_{bat}) and the DC-bus voltage (V_{bus}), the power flow direction can be determined. Power transfer can then be realized by adequately controlling the power switches. Moreover, the proposed converter can achieve ZVS and obtain high efficiency through a novel modulation strategy.

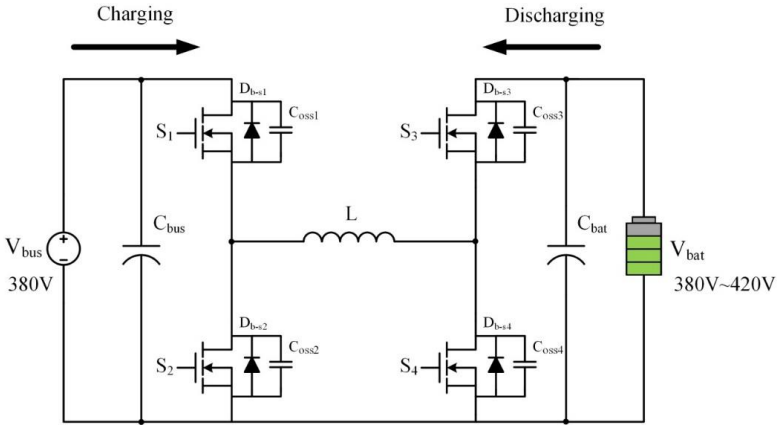

Figure 1. Circuit diagram of the universal bidirectional DC-DC converter.

The charging/discharging mode here is defined as that the energy is transferred from the DC-bus/battery to the battery/DC-bus. Since the battery voltage may be higher or lower than the DC-bus voltage during the entire operation, there exist four operation modes as follows: boost-charging, buck-charging, boost-discharging and buck-discharging. Figure 2 illustrates the key waveforms of the boost/buck-charging mode, and the waveforms of the buck/boost-discharging mode are shown in Figure 3.

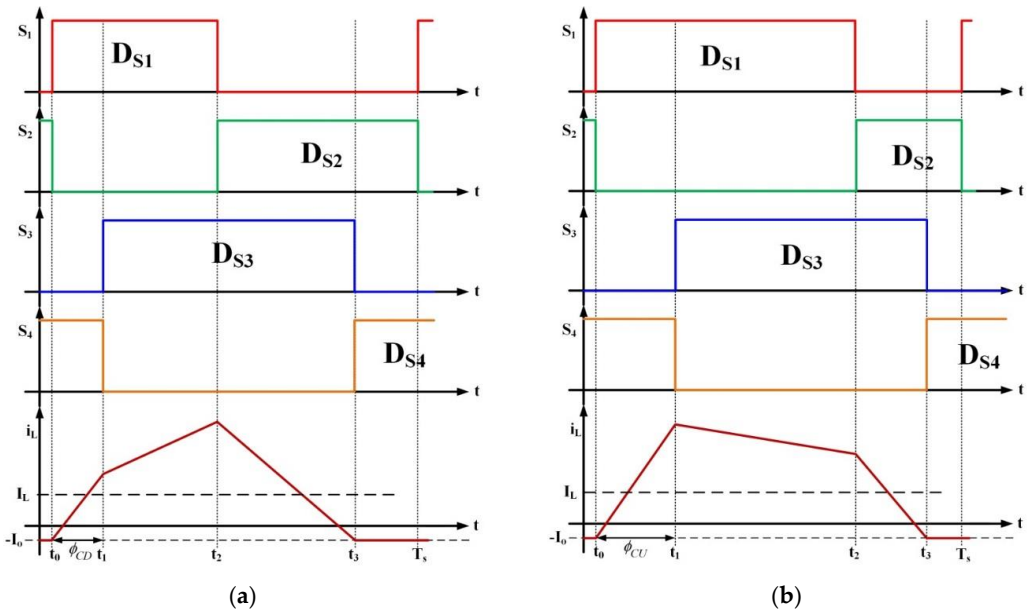

Figure 2. The gating signals and inductor current waveforms during charging operation. (**a**) Buck mode; (**b**) Boost mode.

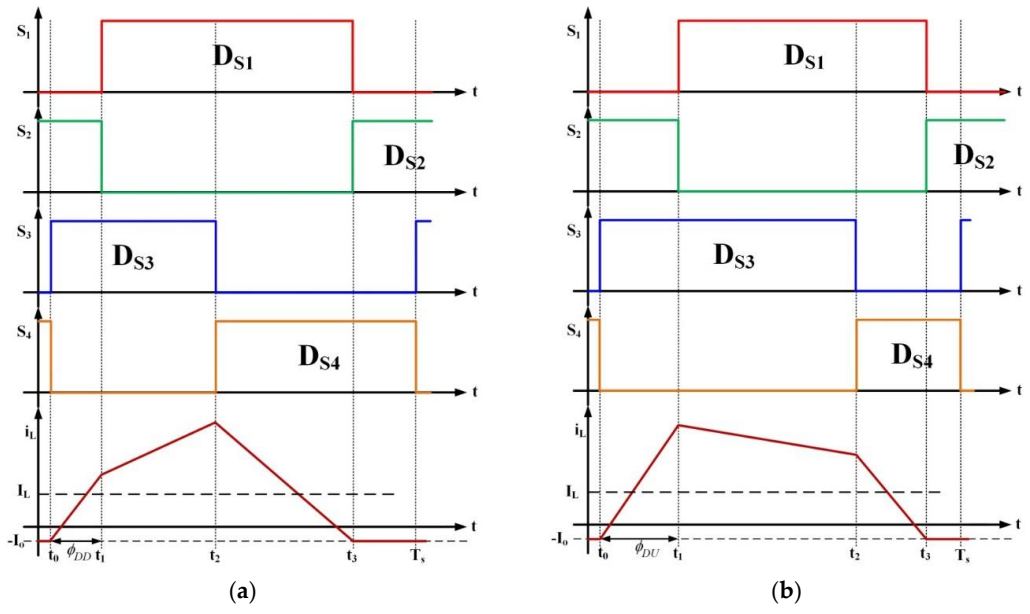

Figure 3. The gating signals and inductor current waveforms during discharging operation. (**a**) Buck mode; (**b**) Boost mode.

The required gating signals of these four operation modes are summarized in Table 1. The operating principles for both buck-boost charging and buck-boost discharging modes are similar.

Therefore, only circuit operation under the buck-charging mode is analyzed and discussed with the following assumptions:

1. All components are ideal except switching devices;
2. There is no trace resistance;
3. Capacitance is very large such that capacitor voltage can be considered constant.

Table 1. The gating signals required for four operating modes.

Mode	Buck Mode	Boost Mode
Charging mode	Shown in Figure 2a Gating signals for S_1, S_2 and S_3, S_4 are complementary Duty cycle of S_3 and S_4 is 50% Duty cycle of S_1 varies and should be lower than 50% There is a phase-shift ϕ between S_3 and S_1 (S_3 lagging) Voltage conversion ratio equals D_{S1}/D_{S3}	Shown in Figure 2b Gating signals for S_1, S_2 and S_3, S_4 are complementary Duty cycle of S_3 and S_4 is 50% Duty cycle of S_1 varies and should be greater than 50% There is a phase-shift ϕ between S_3 and S_1 (S_3 lagging) Voltage conversion ratio equals D_{S1}/D_{S3}
Discharging mode	Shown in Figure 3a Gating signals for S_1, S_2 and S_3, S_4 are complementary Duty cycle of S_1 and S_2 is 50% Duty cycle of S_3 varies and should be lower than 50% There is a phase-shift ϕ between S_1 and S_3 (S_1 lagging) Voltage conversion ratio equals D_{S3}/D_{S1}	Shown in Figure 3b Gating signals for S_1, S_2 and S_3, S_4 are complementary Duty cycle of S_1 and S_2 is 50% Duty cycle of S_3 varies and should be greater than 50% There is a phase-shift ϕ between S_1 and S_3 (S_1 lagging) Voltage conversion ratio equals D_{S3}/D_{S1}

Figure 4 shows the typical waveforms of the proposed converter operating under buck-charging mode. From Figure 4, the whole operation can be divided into 12 time intervals, as described below:

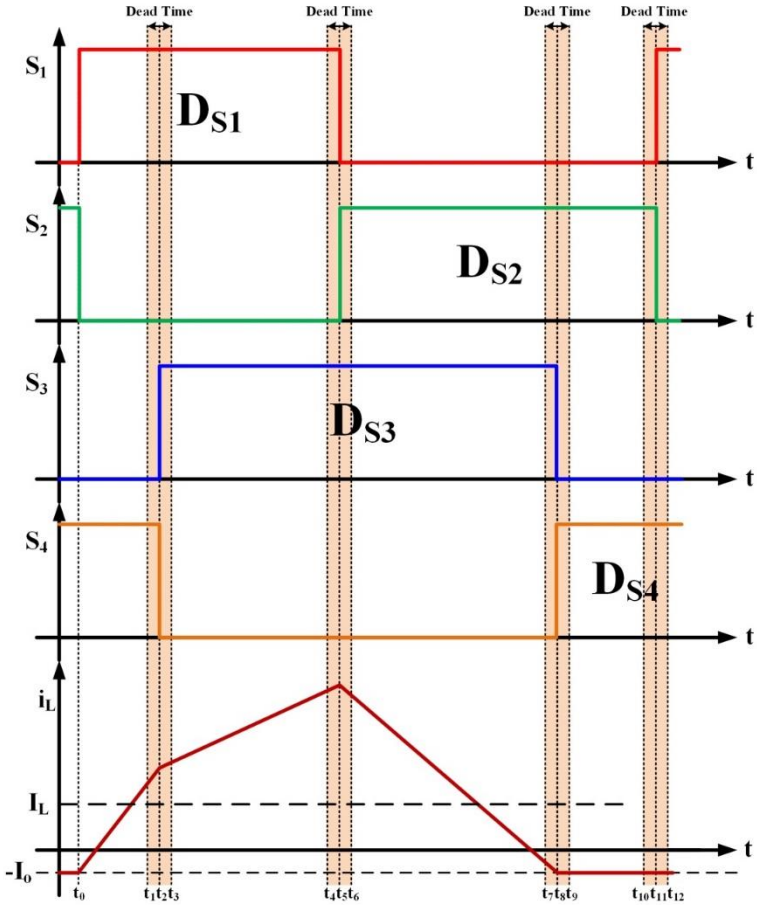

Figure 4. Typical waveforms of buck-charging mode.

Interval 1 ($t_0 \leqslant t < t_1$): At $t = t_0$, power switch S_1 is turned on with ZVS since the body diode $D_{b\text{-}s1}$ has already been conducting in prior. During this time interval, power switches S_1 and S_4 are on and

S_2, S_3 are off, the equivalent circuit is shown in Figure 5a. The voltage across the inductor is the dc-bus voltage V_{bus} and the inductor current increases linearly. The load power is supplied by the capacitor C_{bat} solely.

Interval 2 ($t_1 \leqslant t < t_2$): At $t = t_1$, power switch S_4 is turned off. During this time interval, power switch S_1 is on and S_2, S_3, S_4 are off, the equivalent circuit is shown in Figure 5b. Since the inductor current cannot change abruptly, it discharges the parasitic capacitor C_{oss3} and charges the parasitic capacitor C_{oss4}. When the voltage across C_{oss3} becomes zero, the body diode $D_{b\text{-}s3}$ conducts. This positions S_3 with no drain to source voltage prior to turn-on and facilitates ZVS.

Interval 3 ($t_2 \leqslant t < t_3$): At $t = t_2$, the body diode $D_{b\text{-}s3}$ conducts. During this time interval, power switch S_1 is on and S_2, S_3, S_4 are off, the equivalent circuit is shown in Figure 5c. The load power is supplied by the dc-bus through power switch S_1 and body diode $D_{b\text{-}s3}$.

Interval 4 ($t_3 \leqslant t < t_4$): At $t = t_3$, power switch S_3 is turned on with ZVS. During this time interval, power switches S_1 and S_3 are on and S_2, S_4 are off, the equivalent circuit is shown in Figure 5d. The voltage across the inductor equals to the difference of the DC-bus voltage V_{bus} and the battery voltage V_{bat}. Since V_{bus} is larger than V_{bat} in buck-charging mode, the voltage difference is still positive and the inductor current increases linearly with a smaller slope. The load power is supplied by the dc-bus through power switches S_1 and S_3.

Interval 5 ($t_4 \leqslant t < t_5$): At $t = t_4$, power switch S_1 is turned off. During this time interval, power switch S_3 is on and S_1, S_2, S_4 are off, the equivalent circuit is shown in Figure 5e. Since the inductor current cannot change abruptly, it charges the parasitic capacitor C_{oss1} and discharges the parasitic capacitor C_{oss2}. When the voltage across C_{oss2} becomes zero, the body diode $D_{b\text{-}s2}$ conducts.

Interval 6 ($t_5 \leqslant t < t_6$): At $t = t_5$, the body diode $D_{b\text{-}s2}$ conducts. During this time interval, power switch S_3 is on and S_1, S_2, S_4 are off, the equivalent circuit is shown in Figure 5f. The load power is supplied by the inductor through power switch S_3 and body diode $D_{b\text{-}s2}$.

Interval 7 ($t_6 \leqslant t < t_7$): At $t = t_6$, power switch S_2 is turned on with ZVS. During this time interval, power switches S_2 and S_3 are on and S_1, S_4 are off, the equivalent circuit is shown in Figure 5g. The voltage across the inductor equals to $-V_{bat}$ and the inductor current decreases linearly. The load power is supplied by the inductor through power switches S_2 and S_3. It should be noted that a negative inductor offset current $-I_0$ is needed for allowing power switch S_4 to turn on with ZVS.

Interval 8 ($t_7 \leqslant t < t_8$): At $t = t_7$, power switch S_3 is turned off. During this time interval, power switch S_2 is on and S_1, S_3, S_4 are off, the equivalent circuit is shown in Figure 5h. Since the inductor current cannot change abruptly, it charges the parasitic capacitor C_{oss3} and discharges the parasitic capacitor C_{oss4}. When the voltage across C_{oss4} becomes zero, the body diode $D_{b\text{-}s4}$ conducts.

Interval 9 ($t_8 \leqslant t < t_9$): At $t = t_8$, the body diode $D_{b\text{-}s4}$ conducts. During this time interval, power switch S_2 is on and S_1, S_3, S_4 are off, the equivalent circuit is shown in Figure 5i. The load power is supplied by the capacitor C_{bat} solely.

Interval 10 ($t_9 \leqslant t < t_{10}$): At $t = t_9$, power switch S_4 is turned on with ZVS. During this time interval, power switches S_2 and S_4 are on and S_1, S_3 are off, the equivalent circuit is shown in Figure 5j. The voltage across the inductor is zero and the inductor current is kept constant. The load power is supplied by the capacitor C_{bat} solely.

Interval 11 ($t_{10} \leqslant t < t_{11}$): At $t = t_{10}$, power switch S_2 is turned off. During this time interval, power switch S_4 is on and S_1, S_2, S_3 are off, the equivalent circuit is shown in Figure 5k. Since the inductor current cannot change abruptly, it discharges the parasitic capacitor C_{oss1} and charges the parasitic capacitor C_{oss2}. When the voltage across C_{oss1} becomes zero, the body diode $D_{b\text{-}s1}$ conducts.

Interval 12 ($t_{11} \leqslant t < t_{12}$): At $t = t_{11}$, the body diode $D_{b\text{-}s1}$ conducts. During this time interval, power switch S_4 is on and S_1, S_2, S_3 are off, the equivalent circuit is shown in Figure 5l. The load power is supplied by the capacitor C_{bat} solely.

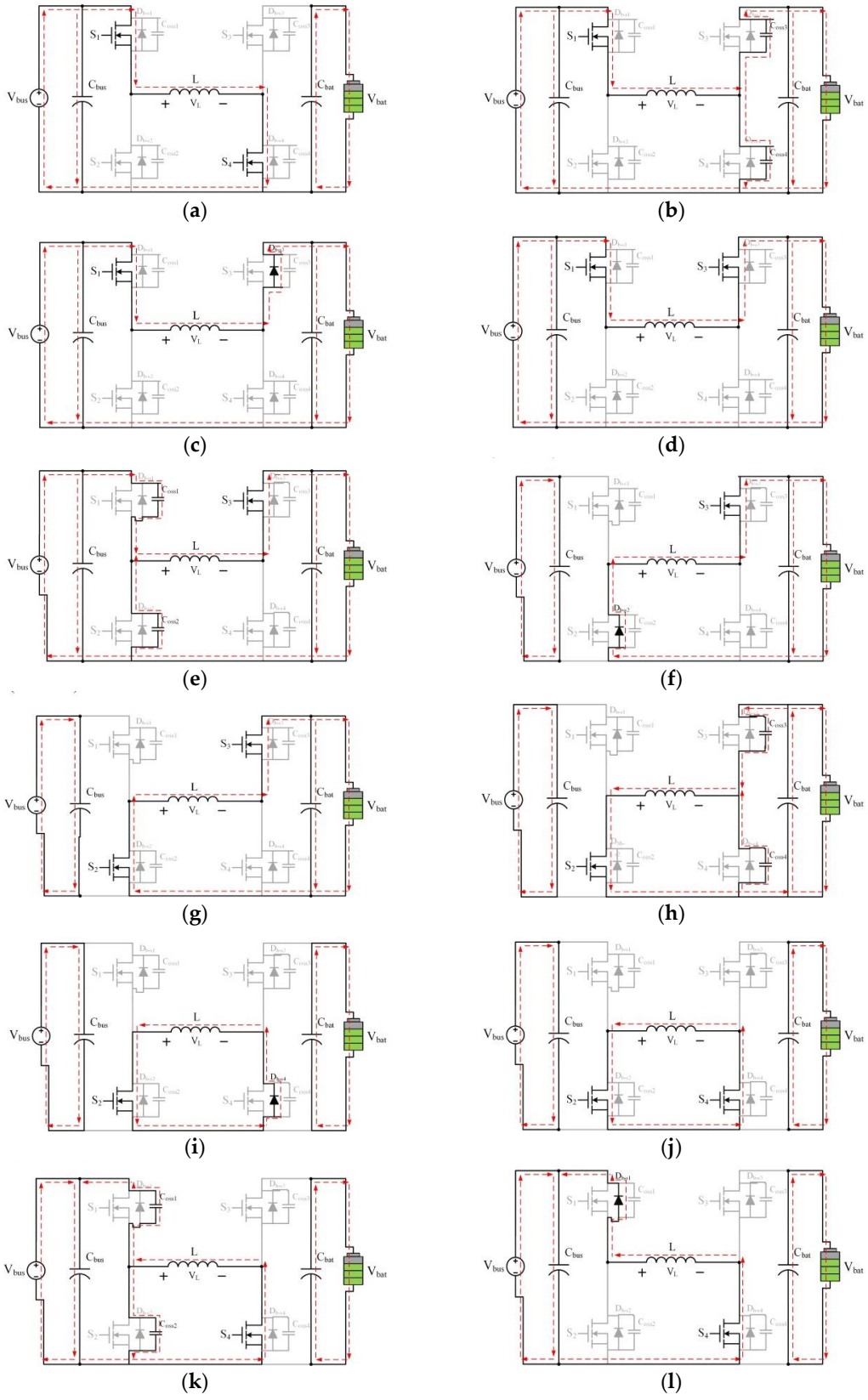

Figure 5. Equivalent circuits of different time intervals for buck-charging mode. (**a**) Interval 1; (**b**) Interval 2; (**c**) Interval 3; (**d**) Interval 4; (**e**) Interval 5; (**f**) Interval 6; (**g**) Interval 7; (**h**) Interval 8; (**i**) Interval 9; (**j**) Interval 10; (**k**) Interval 11; (**l**) Interval 12.

3. The Proposed Adaptive Phase-Shift Control Method

Since the system efficiency will be affected by the phase-shift angle and the inductance, the relationship between these two factors needed to be derived first. From the circuit analysis presented in Section 2, the time function of inductor current shown in Figure 2a can be derived as:

$$i_L(t) = \begin{cases} -I_o + \frac{V_{bat}}{L}t & for\ t_0 \leqslant t \leqslant t_1 \\ -I_o + \frac{V_{bus}}{L}t_1 + \frac{V_{bat}-V_{bus}}{L}t & for\ t_1 \leqslant t \leqslant t_2 \\ -I_o + \frac{V_{bus}}{L}t_1 + \frac{V_{bat}}{L}t_2 - \frac{V_{bus}}{L}t & for\ t_2 \leqslant t \leqslant t_3 \\ -I_o & for\ t_3 \leqslant t \leqslant T_s \end{cases} \quad (1)$$

The average power P_{average} can be defined as Equation (2). By substituting Equation (1) into Equation (2), the average input power (P_{in}) and the average output power (P_{out}) can be obtained as:

$$P_{average} = \frac{1}{T_s}\int_0^{T_s} v(t)\cdot i(t)dt \quad (2)$$

$$\begin{aligned} P_{in} &= \frac{V_{bus}}{T_s}\int_{t_0}^{t_2} i_L(t)dt \\ &= \frac{V_{bus}}{2T_sL}\left[-V_{bus}t_1^2 + (V_{bus}-V_{bat})\,t_2^2 + 2V_{bus}t_1t_2\right] - \frac{V_{bat}I_o}{T_s}t_2 \end{aligned} \quad (3)$$

$$\begin{aligned} P_{out} &= \frac{V_{bat}}{T_s}\int_{t_1}^{t_3} i_L(t)dt \\ &= \frac{V_{bus}}{2T_sL}\left[-(V_{bus}+V_{bat})\,t_1^2 - V_{bat}t_2^2 - V_{bus}t_3^2 + V_{bus}t_1t_3 + 2V_{bat}t_2t_3\right] - \frac{V_{bus}I_o}{T_s}(t_3-t_1) \end{aligned} \quad (4)$$

From Equations (3) and (4), it can be noted that the input power and output power are related to the switching times, t_1, t_2 and t_3. Thus, the maximum average power can be obtained once the optimal values of t_1, t_2, and t_3 are determined. Assuming the power switches are ideal which means that the converter losses can be neglected, the input power and the output power should be equal to the average power, as shown in Equation (5):

$$P_{in} = P_{out} = P_{average} \quad (5)$$

From Figure 2a, it can be found that when $t = t_3$, the inductor current is equal to $-I_o$, as described in Equation (6). From Equation (6), the relationship between t_1 and t_2 can be obtained as Equation (7).

$$i_L(t_3) = -I_o + \frac{V_{bus}}{L}t_1 + \frac{V_{bat}}{L}t_2 - \frac{V_{bus}}{L}t_3 = -I_o \quad (6)$$

$$\begin{aligned} t_1 &= \frac{V_{bat}}{V_{bus}}(t_3 - t_2) \\ t_2 &= \frac{V_{bus}}{V_{bat}}(t_3 - t_1) \end{aligned} \quad (7)$$

By substituting Equation (7) into Equations (3) and (4), the average power $P_{\text{average}}(t_1)$ and $P_{\text{average}}(t_2)$ can be derived. Let both $\frac{dP_{\text{average}}(t_1)}{dt}$ and $\frac{dP_{\text{average}}(t_2)}{dt}$ equal to zero, $t_{1,\max}$ and $t_{2,\max}$ can be calculated as:

$$\begin{aligned} t_{1,\max} &= \frac{V_{bus}^2 t_3 + V_{bat}I_oL}{V_{bus}^2 + V_{bus}V_{bat} + V_{bat}^2} \\ t_{2,\max} &= \frac{(V_{bus}^2 + V_{bus}V_{bat})t_3 - V_{bat}I_oL}{V_{bus}^2 + V_{bus}V_{bat} + V_{bat}^2} \end{aligned} \quad (8)$$

Hence, from Equations (3) and (8), the maximum average power $P_{\text{average,max}}$ can be derived as:

$$P_{\text{average,max}} = V_{bus}V_{bat}\frac{\left[I_o^2L^2 - 2I_oL\,(V_{bus}+V_{bat})\,t_3 + V_{bus}V_{bat}t_3^2\right]}{2\cdot L\cdot T_s\left(V_{bus}^2 + V_{bus}V_{bat} + V_{bat}^2\right)} \quad (9)$$

According to Equation (9), the required inductance can be calculated from any specified operating voltage and maximum average power.

Next, the derivation of the proposed adaptive phase-shift (APS) control method will be detailed. Take Figure 2a for example, the relationship between t_3 and ϕ can be derived as:

$$\phi = 360 \cdot (\frac{t_3}{T_s} - 0.5) \tag{10}$$

According to Equations (9) and (10), it can be noticed that the phase-shift angle varies with the length of t_3 under different load conditions. Furthermore, the phase-shift angle is related to the maximum output power of the universal bidirectional DC-DC converter. Figure 6 shows the inductor current waveform under different load conditions when phase-shift angle is fixed.

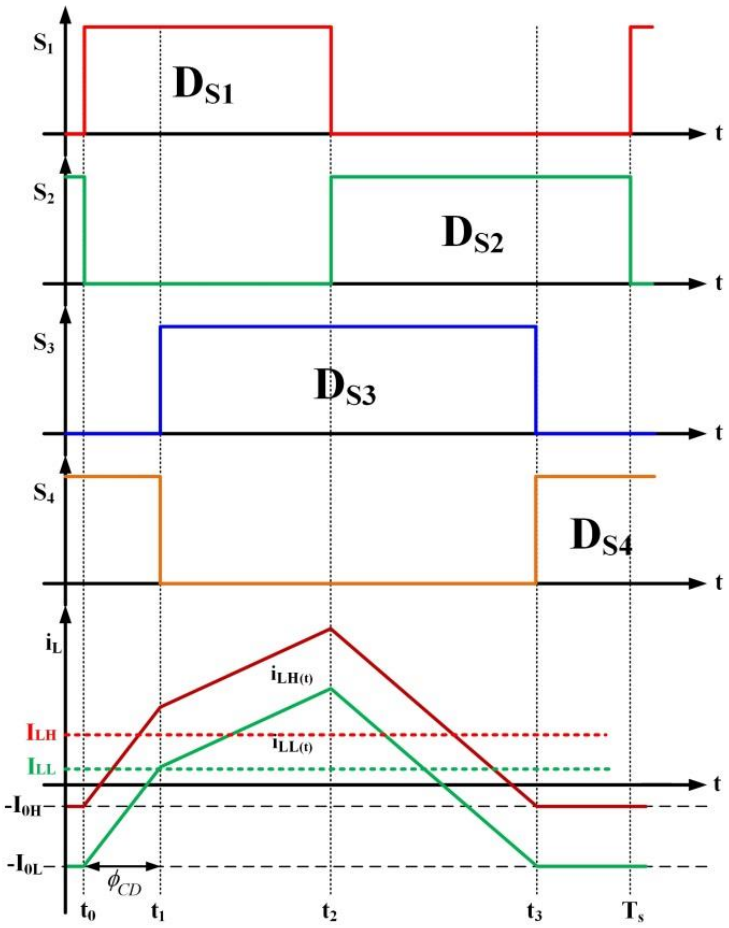

Figure 6. Inductor current waveform under different load conditions (ϕ fixed).

In Figure 6, $i_{LH}(t)$ and $i_{LL}(t)$ correspond to inductor current under heavy load and light load, respectively. Also in Figure 6, the average value of $i_{LH}(t)$ and $i_{LL}(t)$ is I_{LH} and I_{LL} ($I_{LH} > I_{LL}$), respectively. From Figure 6, due to the fixed phase-shift φ, the peak-to-peak inductor current of both light load and heavy load are the same, but the lowest value of $i_{LL}(t)$ (I_{0L}) is smaller than that of $i_H(t)$ (I_{0H}). When the load increases, the lowest point of the inductor current also increases. However, as described in Section 2, a negative inductor offset current $-I_0$ is needed for power switches S_1 and S_4 to achieve ZVS. Therefore, if ZVS for all power switches is required, the maximum load current provided by a fixed phase-shift φ will also be limited to a fixed value. For designing I_0 value, since

the energy stored in the inductor should be large enough to completely transfer the charge stored in MOSFET parasitic capacitance, the design equation of I_0 can be written as:

$$I_0 \geqslant \max(V_{\text{bus,max}}, V_{\text{bat,max}}) \cdot \sqrt{\frac{C_{OSS}}{L}} \tag{11}$$

Figure 7 shows the inductor current waveform under the same load, input voltage and output voltage but different phase-shift ϕ, with $i_A(t)$, $i_B(t)$, $i_C(t)$ corresponding to the phase-shift values of ϕ_A, ϕ_B and ϕ_C, respectively. From Figure 7, the average values of $i_A(t)$, $i_B(t)$ and $i_C(t)$ are all equal to the same load current I_L. However, under different phase-shift values, the peak-to-peak inductor currents appear to be different. To achieve ZVS, the inductor current is required to be negative at $t = t_3$; therefore, ZVS can be achieved for all waveforms in Figure 7. However, it can also be seen from Figure 7 that an excessive phase-shift forces the peak-to-peak inductor current to increase, causing the increases of the conduction loss and the power loss in the inductor. Hence, an adaptive phase-shift (APS) control method is proposed in this paper. In this method, the phase-shift value is automatically adjusted according to the output load. Since a lower root-mean-square (RMS) current flowing through the inductor can effectively decrease the converter losses while still ensure the ZVS operation for all power switches if the inductor offset current $-I_0$ remains negative. Therefore, there exists an optimal phase-shift value which can keep the $|I_0|$ minimum.

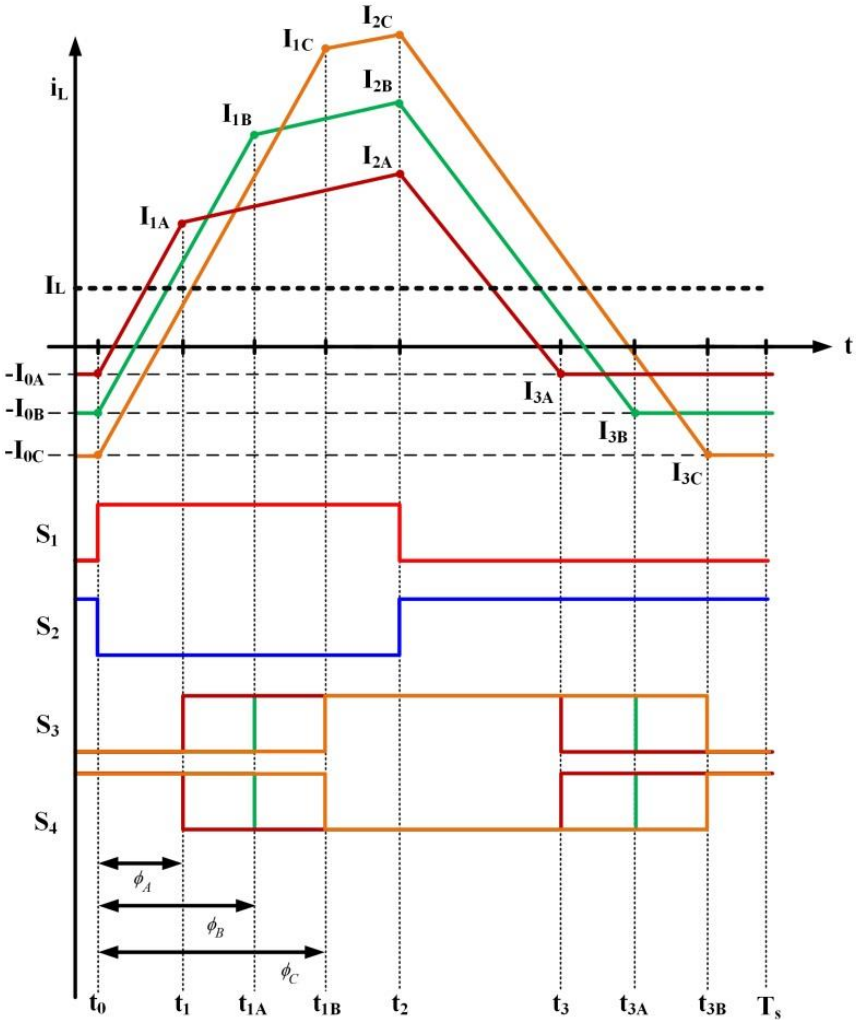

Figure 7. Inductor current waveform under different phase-shift ϕ (other operating conditions fixed).

The flow chart of the proposed APS method is shown in Figure 8. From Figure 8, the operating principle of the proposed method is similar to that of perturb and observe method, and can be described as follows: When the load increases, the phase-shift value is increased by a fixed step $\Delta\phi$ (1° in this paper) and the value of the inductor current at $t = t_3$ is measured. The phase-shift increment will continue until the inductor offset current is turned from negative to positive. The phase-shift value of previous instance is then recorded and set as the optimal value under this load condition. Likewise, when the load decreases, the phase-shift ϕ is reduced by a fixed step $\Delta\phi$ until the inductor offset current turns from positive to negative. With this APS control method, the proposed universal bidirectional DC-DC converter can achieve ZVS under a wide range of load conditions. Comparing with the conventional fixed phase-shift method, the conversion efficiency under different load conditions can be improved.

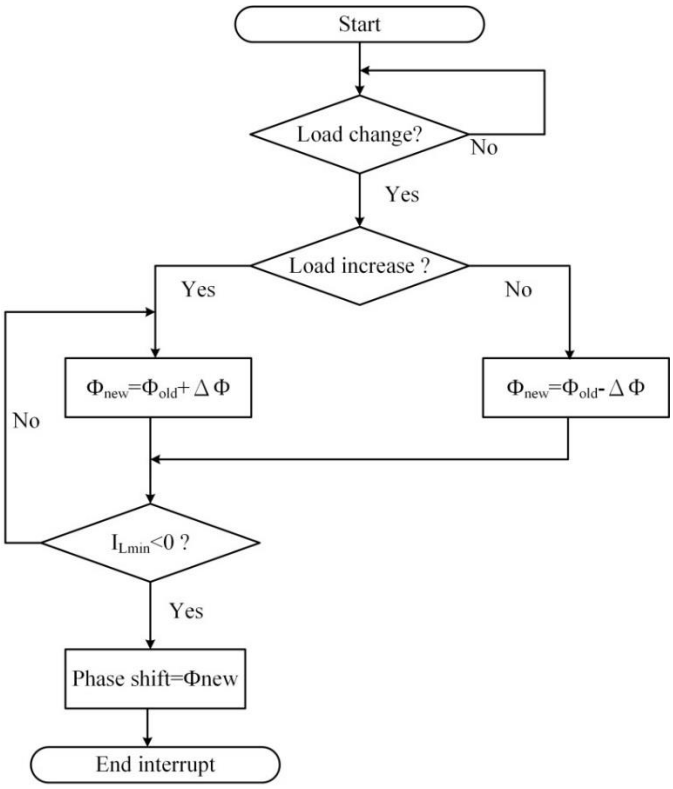

Figure 8. Flowchart of the proposed APS method.

4. Firmware Architecture

The block diagram of the proposed system is shown in Figure 9. In this paper, a dsPIC33FJ16GS502 digital signal controller (DSC) from Microchip Corp. (Chandler, AZ, USA) is adopted to realize the control algorithms. From Figure 9, signal conditioning circuits are used to sense the input voltage, output voltage and output current at first. Analog to digital converter (ADC) is then utilized to convert the analog signals into digital ones. After that, a digital finite impulse response (FIR) filter is applied to remove the noises and the required voltage regulation is carried out via the digital PID compensator. In this way, the dc-bus voltage regulation of the proposed bidirectional DC-DC converter can be achieved.

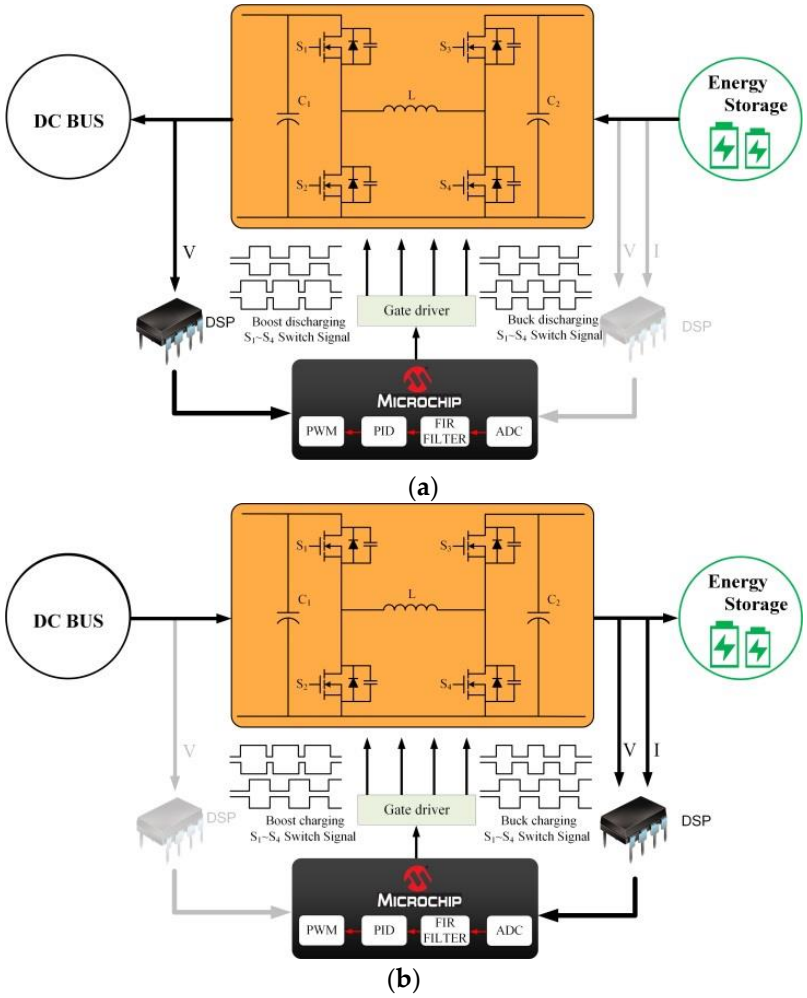

Figure 9. Block diagram of the proposed system.

Figure 10 shows the flowchart of the implemented control algorithm. From Figure 10, the control algorithm for the proposed bidirectional DC-DC converter can be roughly divided into two parts: main program and ADC interrupt subroutine. The required peripheral modules are enabled and initialized at the beginning of the main program. After that, the main program stays in an infinite loop to wait for ADC interrupt to occur. In this paper, the ADC is triggered every 33.3 μs (30 kHz). When the interrupt occurs, the voltage and current at both dc-bus side and battery side are measured and fed into a FIR filter, the filtered results are then utilized to determine the operating modes. If V_{bus} is greater/lower than 380 V, charging/discharging mode will be selected. In addition, a hysteresis comparator with threshold voltage equals to 2 V is used to avoid frequent changing of the operation modes. In discharging mode, if V_{bat} is higher than 380 V, the buck-discharging mode activates; otherwise, the boost-discharging mode is adopted. Similarly, the boost-charging mode will be activated when V_{bat} is higher than 380 V, and buck-charging mode will be adopted when V_{bat} is lower than 380 V. After obtaining the operating modes, the gating signals of these four power switches can be determined via Table 1. Next, the optimal phase-shift value under this load condition can be obtained via the APS control method explained in Section 3. Finally, a new duty cycle can be calculated using the digital PID controller.

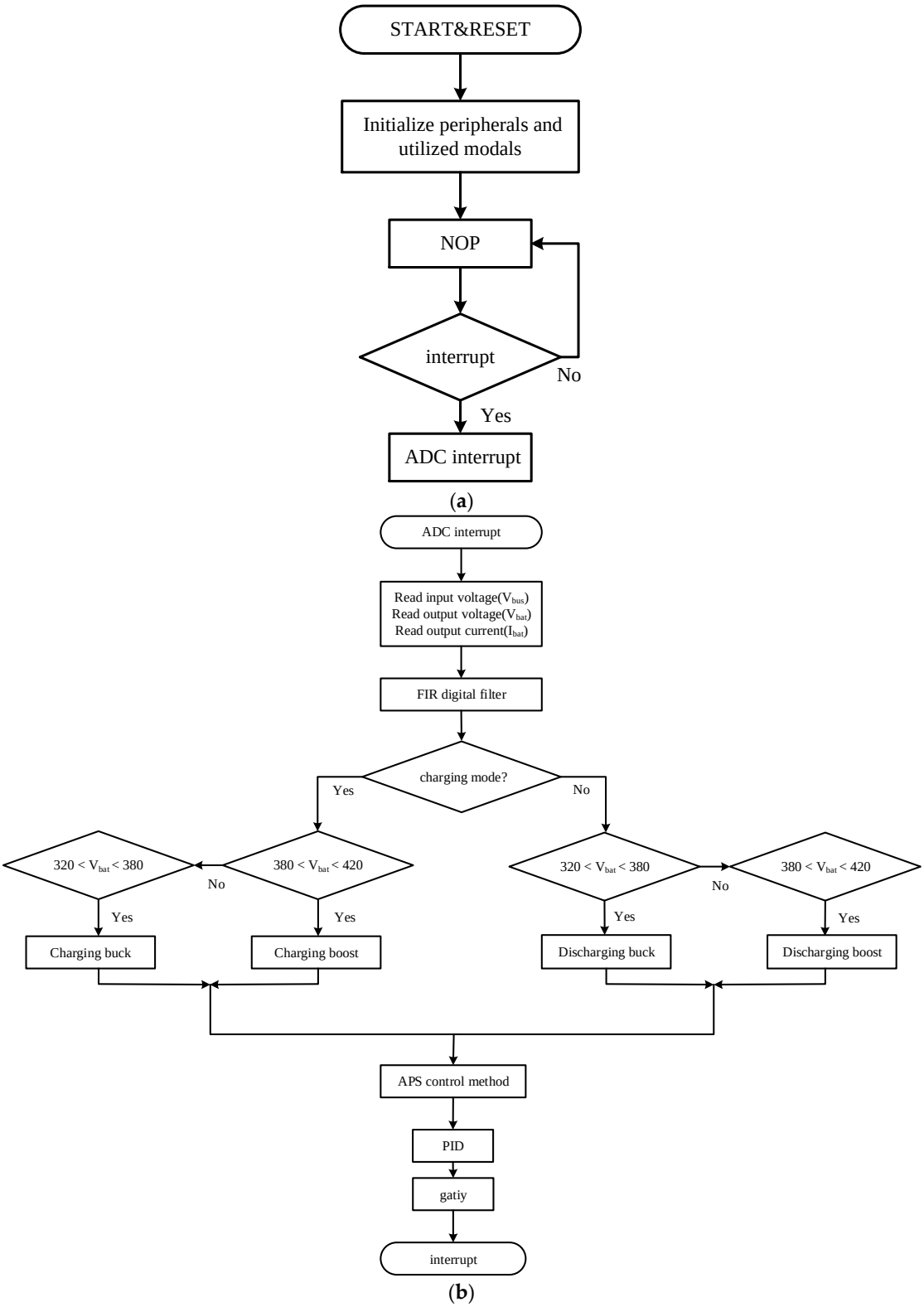

Figure 10. Flowchart of the control algorithm: (**a**) Main program; (**b**) ADC interrupt subroutine.

5. Simulation and Experimental Results

In this paper, PSIM simulation software by POWERSIM Co. (Nyborg, Norway) is applied to verify the feasibility of the proposed universal bidirectional DC-DC converter. Due to space limitation,

only the simulation results under buck-charging mode are provided. The specifications and circuit parameters used in this simulation are listed in Table 2.

Table 2. Specifications and parameter settings of the proposed system.

DC-Bus Voltage (V_{bus})	380 V
Battery voltage (V_{bat})	320–420 V
Switching frequency (f_s)	30 kHz
Inductance (L)	1.5 mH
Capacitance (C_{bus}, C_{bat})	33 μF
Rated power (P_{out})	300 W

Figures 11 and 12 show the simulated results for gating signals and inductor current waveforms under the buck-charging operation at 50 W and 300 W load conditions, respectively. From Figures 11 and 12, the duty cycle of both S_1 and S_2 are 42.1% while the duty cycle of S_3 and S_4 are 50%. It can be observed that the simulated results agree with the theoretical waveforms described in Section 2.

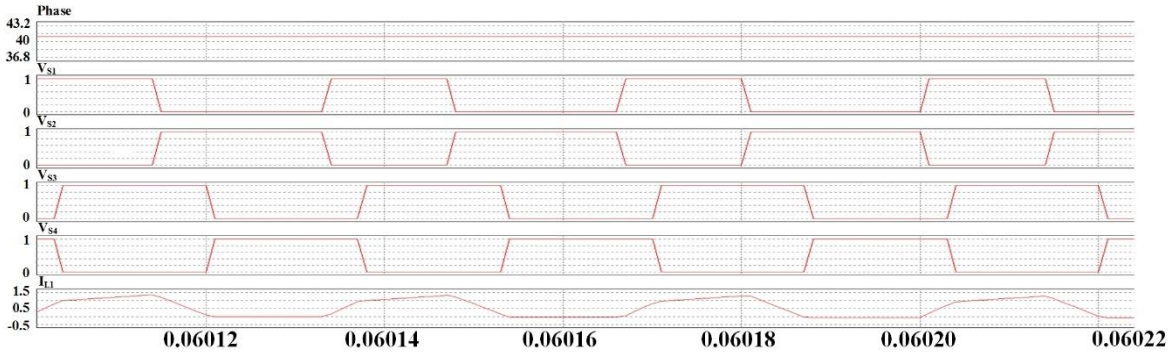

Figure 11. Simulated gating signals and inductor current under buck-charging mode (load = 50 W).

Figure 12. Simulated gating signals and inductor current under buck-charging mode (load = 300 W).

Figure 13 shows the simulated results of the proposed APS control method during a load change (50 W to 300 W). From Figure 13, the phase-shift value between S_3 and S_1 is able to vary with the load to ensure that the inductor offset current is negative and, in consequence, the power switches can be turned on with ZVS.

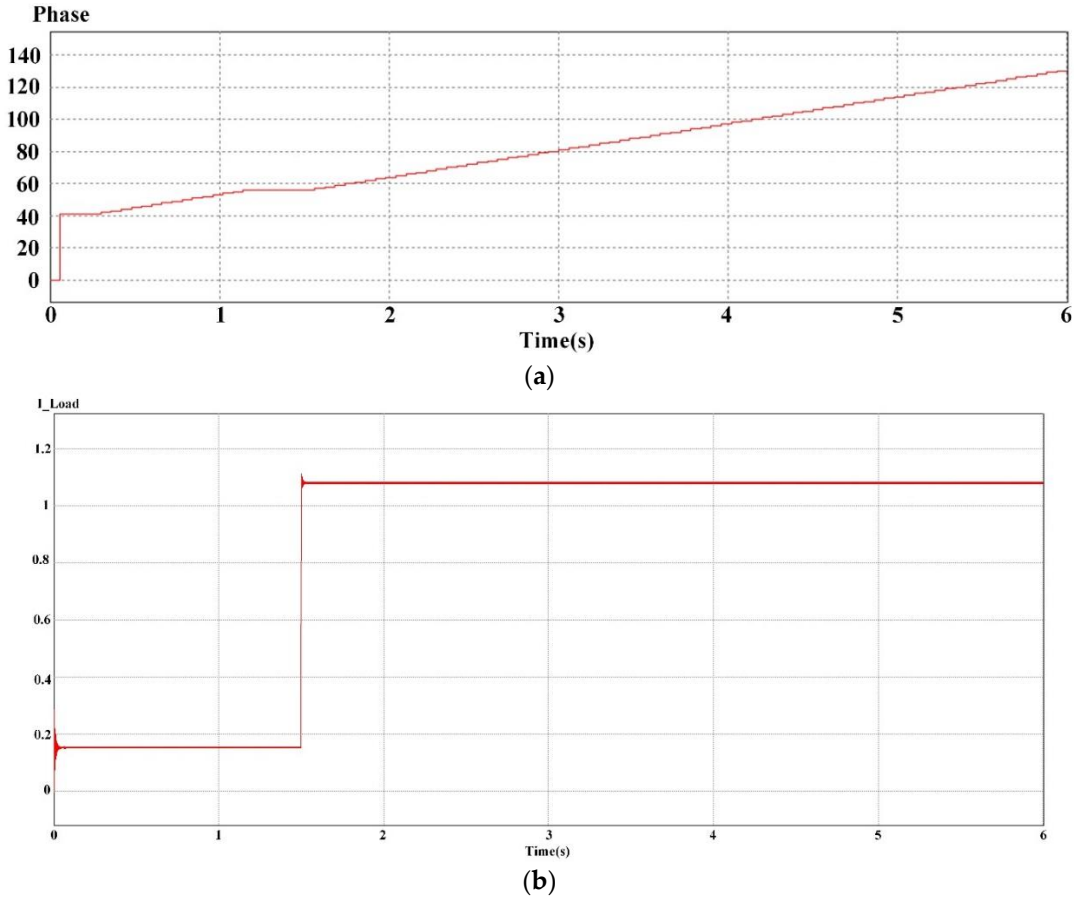

Figure 13. Simulated results of the proposed APS control method during a load change (50 W to 300 W). (**a**) Phase-shift value ϕ; (**b**) Load current.

Next, a prototyping circuit will be constructed and experiments will be carried out to validate the correctness and effectiveness of the proposed method. The specifications and the circuit parameters of the implemented universal bidirectional DC-DC converter are the same with those listed in Table 2. Figures 14 and 15 show the measured waveforms under the charging mode and discharging mode at full load (300 W), respectively. As can be seen from these figures, the full load condition can be achieved under all operating modes. Since the operating principles for each mode are similar; therefore, only circuit operation under the buck-charging mode is analyzed and discussed.

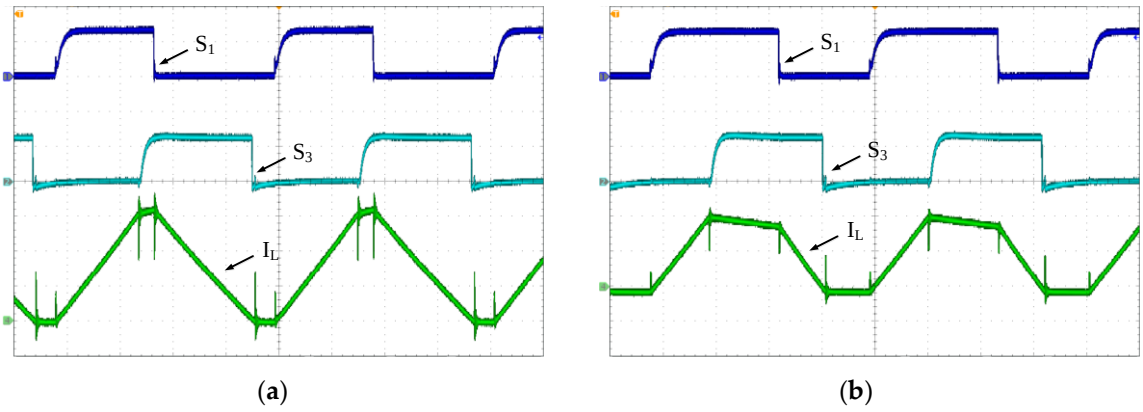

Figure 14. Measured waveforms under charging mode (300 W). (**a**) Buck-charging mode; (**b**) Boost-charging mode.

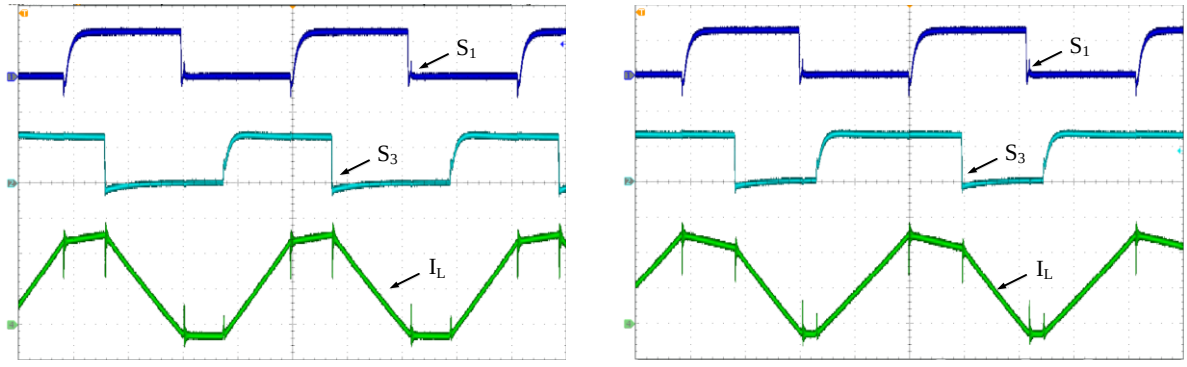

(**a**) (**b**)

Figure 15. Measured waveforms under discharging mode (300 W). (**a**) Buck-discharging mode; (**b**) Boost-discharging mode. (CH1: 10 V/div, CH2: 10 V/div, CH4: 1 A/div, Time: 8 μs/div).

Figure 16 shows the measured current waveforms at different load conditions with the phase-shift value fixed at 148°. From Figure 16, the experimental results agree with the theoretical and the simulated waveforms. Moreover, it can easily be observed that when operated with fixed phase-shift value, the inductor offset current under light-load condition will be lower than that under full-load condition.

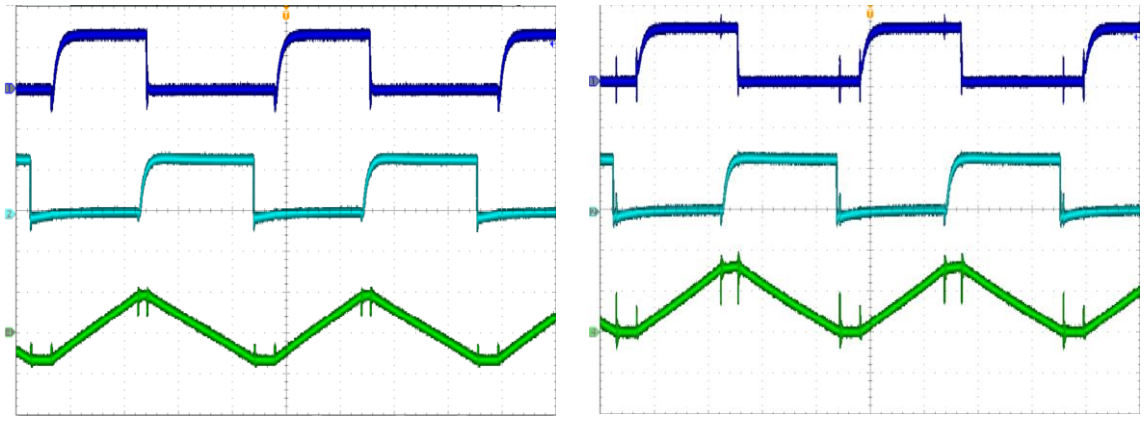

(**a**) (**b**)

Figure 16. Measured waveforms under fixed phase-shift value (148°). (**a**) 50 W; (**b**) 300 W. (CH1: 10 V/div, CH2: 10 V/div, CH4: 1 A/div, Time: 8 μs/div).

Figures 17 and 18 show the measured gating signals and current waveforms using different control methods under 50 W and 250 W load conditions, respectively. In both figures, Figures 17a and 18a are obtained using the proposed APS control method, while Figures 17b and 18b are obtained using the conventional fixed phase-shift value method. It can be seen from Figures 17 and 18 that the peak-to-peak values of the inductor currents using the proposed APS method are all lower than those by the conventional method. As a result, it becomes the main reason of the efficiency improvement.

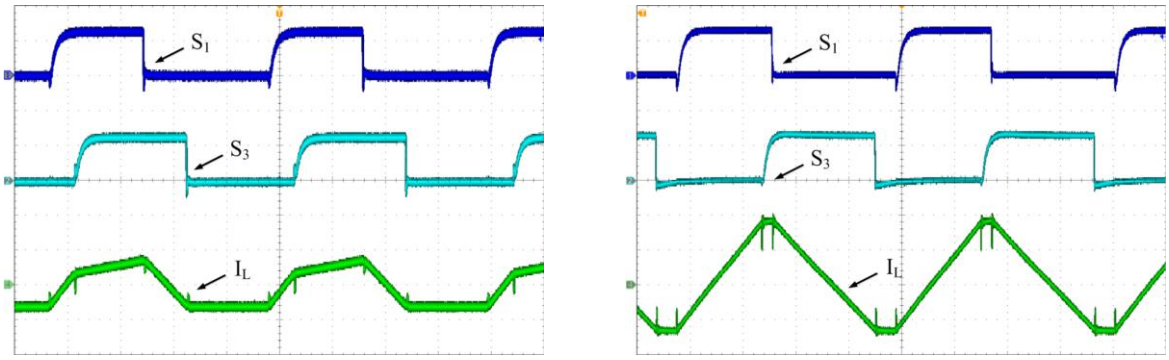

(**a**) (**b**)

Figure 17. Measured waveforms using different control methods (50 W). (**a**) Proposed APS control method (41°); (**b**) Fixed phase-shift value (148°). (CH1: 10 V/div, CH2: 10 V/div, CH4: 1 A/div, Time: 8 μs/div).

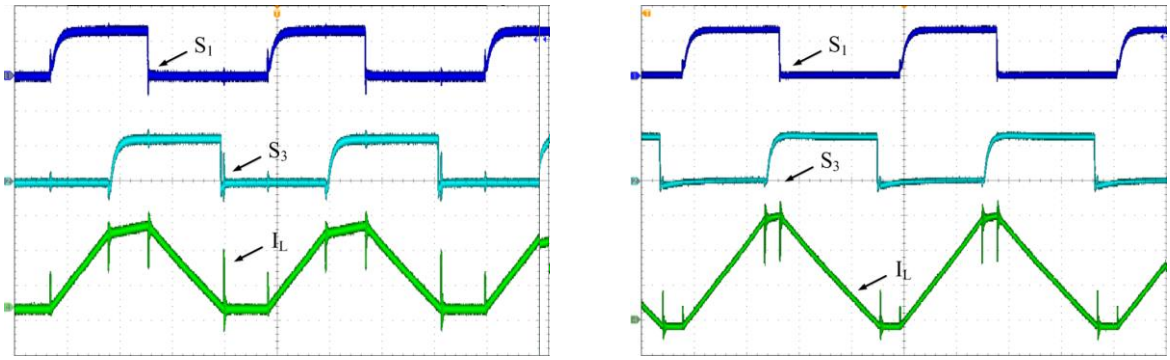

(**a**) (**b**)

Figure 18. Measured waveforms using different control methods (250 W). (**a**) Proposed APS control method (99°); (**b**) Fixed phase-shift value (148°). (CH1: 10 V/div, CH2: 10 V/div, CH4: 1 A/div, Time: 8 μs/div).

Figure 19 shows the measured ZVS turned-on waveforms for power switch S_1 under different load conditions. It is worth noted that with the proposed APS control method, the voltage across the power switch, V_{ds}, can successfully drop to zero regardless of the load conditions. Therefore, the ZVS turned-on can be achieved and the switching losses can be reduced.

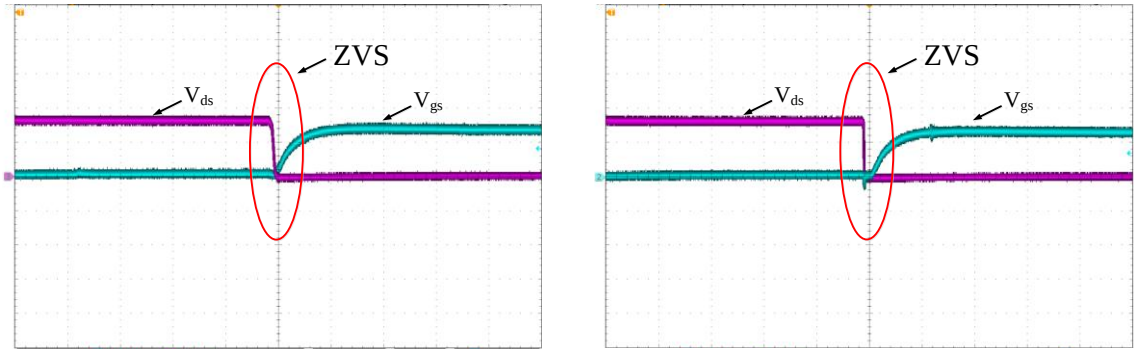

(**a**) (**b**)

Figure 19. Measured ZVS waveforms under different load conditions. (**a**) 50 W; (**b**) 300 W. (CH1: 10 V/div, CH2: 100 V/div, Time: 800 ns/div)

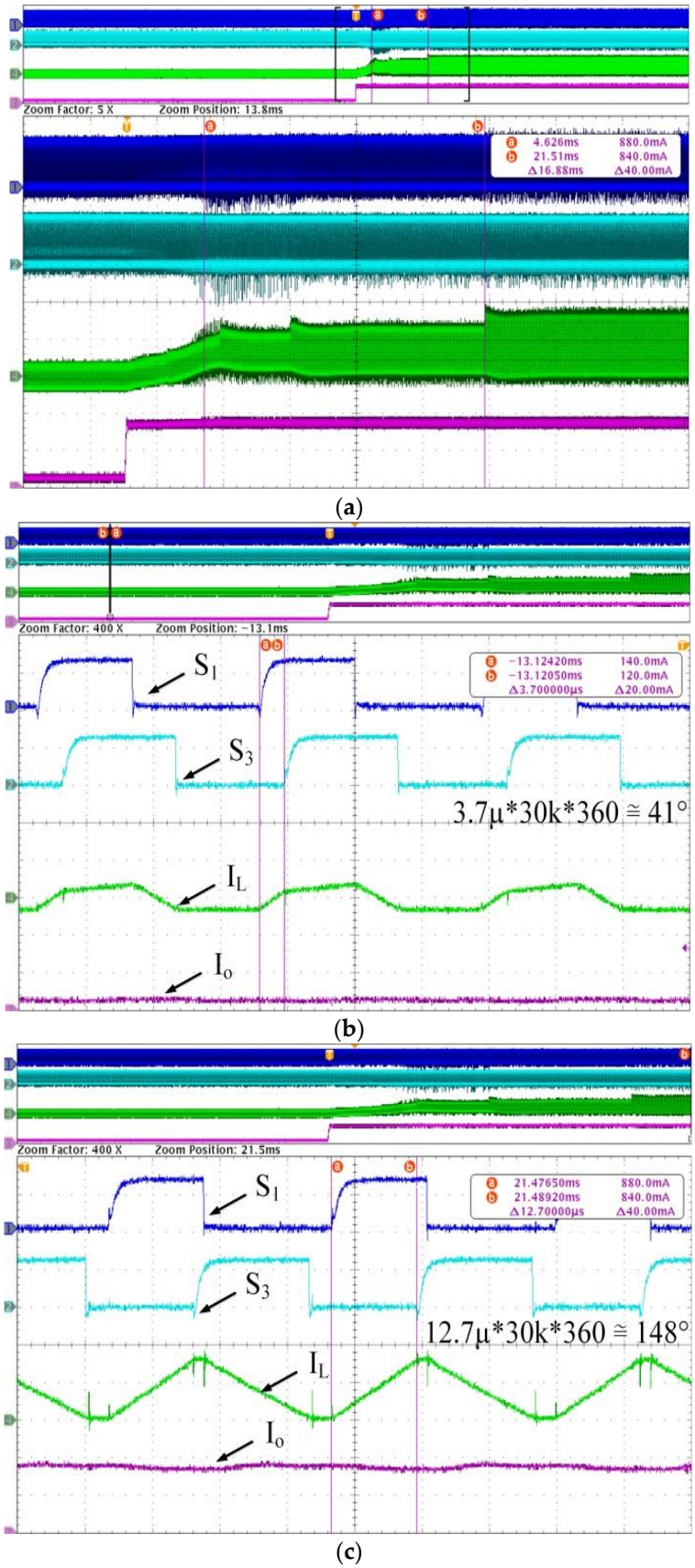

Figure 20. Measured waveforms of the proposed APS control method during a load change (50 W to 300 W). (**a**) Full view; (**b**) Enlarged view at 50 W (41°); (**c**) Enlarged view at 300 W (148°). (CH1: 10 V/div, CH2: 10 V/div, CH4: 2 A/div).

Figure 20 shows the measured waveforms of the proposed APS control method during a load change (50 W to 300 W), in which Figure 20a shows the whole view and Figure 20b,c illustrate the enlarged view under 50 W and 300 W loads, respectively. From Figure 20, the phase-shift value between S_3 and S_1 is able to vary with the load to ensure that the power switches can be turned on with ZVS, which agrees with the simulated results.

Figures 21–24 show the measured efficiency curves of the proposed converter under different load conditions with and without the proposed APS control. The numbers above the circles shown represent the optimal phase-shift values found by the APS control method. It can be noticed that the measured efficiencies of the proposed APS control method are better than the conventional method under the full range of load conditions. Figures 21–24, the obtained peak efficiencies are 96.2%, 97.0%, 96.9%, and 97.0% under buck-charging, boost-charging, buck-discharging and boost-discharging operating modes, respectively. Figure 25 shows the efficiency improvement percentage of the proposed APS control method over the conventional one. From Figure 25, an averaged 12.2%, 6.9%, 4.0%, 2.0%, and 1.0% efficiency improvement under 50 W, 100 W, 150 W, 200 W and 250 W load conditions can be achieved. Finally, Figure 26 shows the picture of the implemented converter.

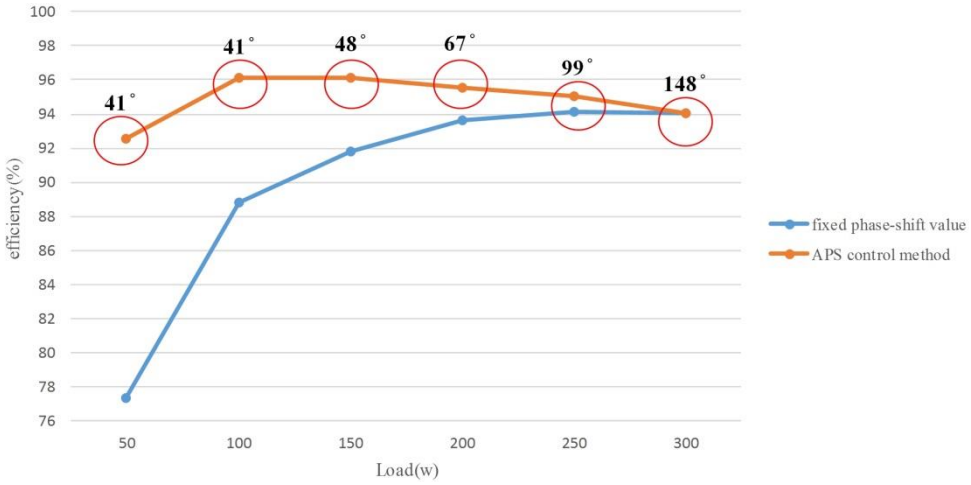

Figure 21. Measured efficiency curves of different control methods under buck-charging mode.

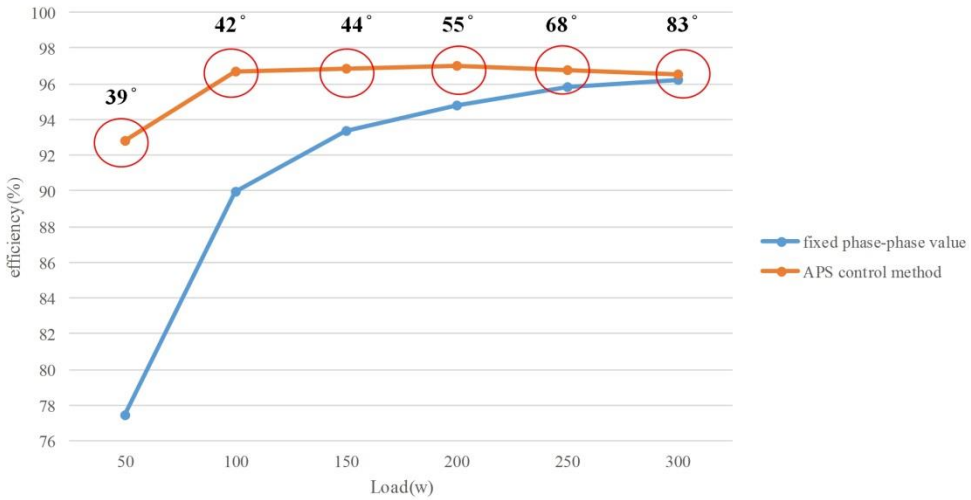

Figure 22. Measured efficiency curves of different control methods under boost-charging mode.

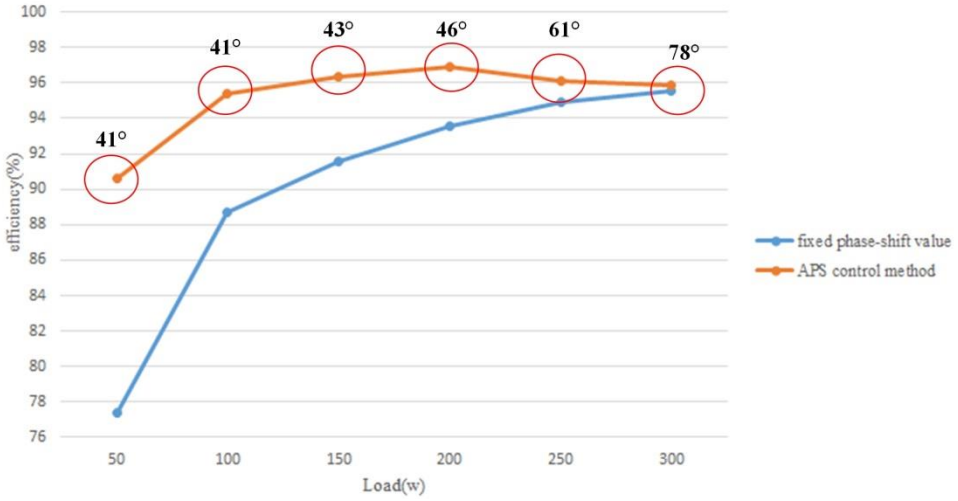

Figure 23. Measured efficiency curves of different control methods under buck-discharging mode.

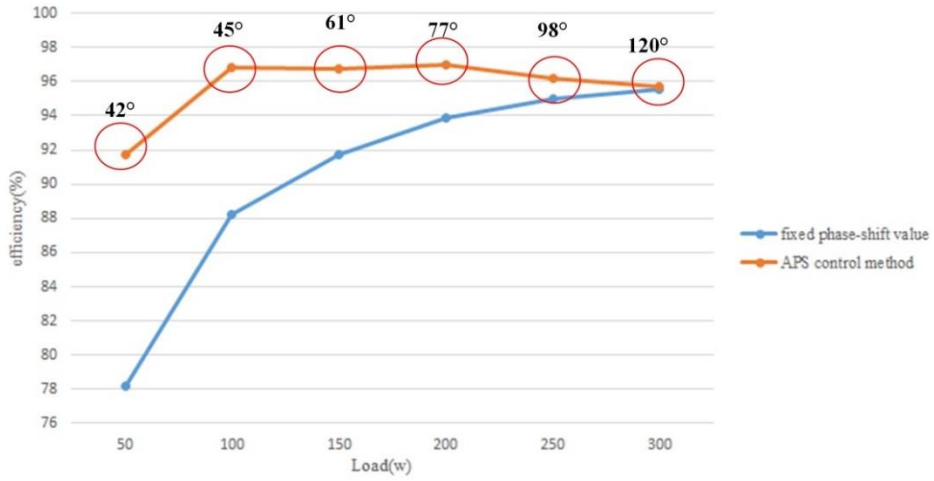

Figure 24. Measured efficiency curves of different control methods under boost-discharging mode.

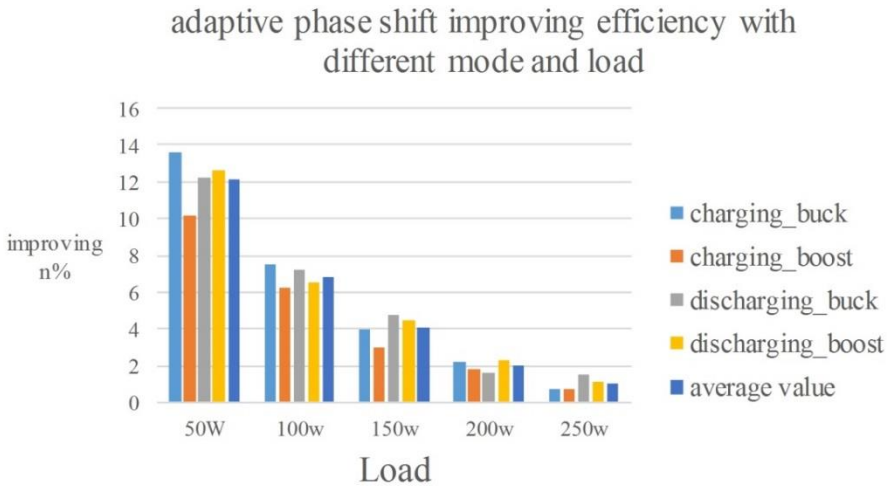

Figure 25. Efficiency improvement of the proposed APS control method under different operating modes.

Figure 26. Picture of the implemented universal bidirectional DC-DC converter.

6. Conclusions

In this paper, a 300 W universal bidirectional DC-DC converter with a digital control algorithm is realized. The advantages of this circuit include simple hardware structure and less passive components. With properly manipulating the gating signals of the four power switches, the direction of the energy flow can easily be controlled; therefore, all the operating modes can be achieved. Moreover, an APS control method is proposed. With this method, the phase-shift value can be adjusted automatically under different load conditions. Using the proposed APS control method, the efficiency under the full range of load conditions can be improved. The proposed universal bidirectional DC-DC converter was simulated and tested to verify the feasibility. According to the experimental results, the obtained maximum efficiencies of these four operating modes are all higher than 96.1%. Moreover, a 12.2% and 4.0% efficiency improvement can be obtained under light load and half load condition, respectively.

Nomenclature

V_{bus}	Bus voltage	V_{bat}	Battery voltage	S_n	Switch, n = 1~4
$D_{b\text{-}sn}$	Body diode of S_n	C_{ossn}	Parasitic capacitor of S_n	L	inductor
C_{bus}	Bus side capacitor	C_{bat}	Battery side capacitor	D_{Sn}	Duty cycle of S_n
ϕ	Phase-shift value	ϕ_{CD}	ϕ of buck-charging mode	ϕ_{CU}	ϕ of boost-charging mode
T_S	Switching period	ϕ_{DD}	ϕ of buck-discharging mode	ϕ_{DU}	ϕ of boost-discharging mode
i_L	Inductor current	I_L	DC value of i_L	I_0	Inductor offset current
P_{in}	Input power	P_{out}	Output power	$P_{average}$	Averaged power
f_s	Switching frequency	V_{ds}	Drain-to-source voltage	V_{gs}	Gate-to-source voltage

References

1. Yang, Y.; Zhang, W.; Jiang, J.; Huang, M.; Niu, L. Optimal Scheduling of a Battery Energy Storage System with Electric Vehicles' Auxiliary for a Distribution Network with Renewable Energy Integration. *Energies* **2015**, *8*, 10718–10735. [CrossRef]
2. Lin, W.M.; Tu, C.S.; Tsai, M.T. Energy Management Strategy for Microgrids by Using Enhanced Bee Colony Optimization. *Energies* **2016**, *9*, 5. [CrossRef]
3. Liu, D.; Wang, Y.; Shen, Y. Electric Vehicle Charging and Discharging Coordination on Distribution Network Using Multi-Objective Particle Swarm Optimization and Fuzzy Decision Making. *Energies* **2016**, *9*, 186. [CrossRef]

4. Shi, X.; Jiang, J.; Guo, X. An Efficiency-Optimized Isolated Bidirectional DC-DC Converter with Extended Power Range for Energy Storage Systems in Microgrids. *Energies* **2013**, *6*, 27–44. [CrossRef]
5. Wang, Z.; Liu, B.; Zhang, Y.; Cheng, M.; Chu, K.; Xu, L. The Chaotic-Based Control of Three-Port Isolated Bidirectional DC/DC Converters for Electric and Hybrid Vehicles. *Energies* **2016**, *9*, 83. [CrossRef]
6. Das, P.; Laan, B.; Mousavi, S.A.; Moschopoulos, G. A Nonisolated Bidirectional ZVS-PWM Active Clamped DC-DC Converter. *IEEE Trans. Power Electron.* **2009**, *24*, 553–558. [CrossRef]
7. Kwon, M.; Oh, S.; Choi, S. High Gain Soft-Switching Bidirectional DC-DC Converter for Eco-Friendly Vehicles. *IEEE Trans. Power Electron.* **2014**, *29*, 1659–1666. [CrossRef]
8. Dusmez, S.; Khaligh, A.; Hasanzadeh, A. A Zero-Voltage-Transition Bidirectional DC/DC Converter. *IEEE Trans. Ind. Electron.* **2015**, *62*, 3152–3162. [CrossRef]
9. Rathore, A.K.; Patil, D.R.; Srinivasan, D. Non-Isolated Bidirectional Soft-Switching Current-Fed LCL Resonant DC/DC Converter to Interface Energy Storage in DC Microgrid. *IEEE Trans. Ind. Appl.* **2016**, *52*, 1711–1722. [CrossRef]
10. Das, P.; Mousavi, S.A.; Moschopoulos, G. Analysis and Design of a Nonisolated Bidirectional ZVS-PWM DC-DC Converter With Coupled Inductors. *IEEE Trans. Power Electron.* **2010**, *25*, 2630–2641. [CrossRef]
11. Sanchis, E.; Maset, E.; Ferreres, A.; Ejea, J.B.; Esteve, V.; Jordan, J.; Calvente, J.; Garrigos, A.; Blanes, J.M. Bidirectional High-Efficiency Nonisolated Step-Up Battery Regulator. *IEEE Trans. Aerosp. Electron. Syst.* **2011**, *47*, 2230–2239. [CrossRef]
12. Do, H.L. Nonisolated Bidirectional Zero-Voltage-Switching DC-DC Converter. *IEEE Trans. Power Electron.* **2011**, *26*, 2563–2569. [CrossRef]
13. Duan, R.Y.; Lee, J.D. High-Efficiency bidirectional DC-DC converter with coupled inductor. *IET Power Electron.* **2012**, *5*, 115–123. [CrossRef]
14. Wu, H.; Lu, J.; Shi, W.; Xing, Y. Nonisolated Bidirectional DC-DC Converters with Negative-Coupled Inductor. *IEEE Trans. Power Electron.* **2012**, *27*, 2231–2235. [CrossRef]
15. Narasimharaju, B.L.; Dubey, S.P.; Singh, S.P. Design and analysis of coupled inductor bidirectional DC-DC convertor for high-voltage diversity applications. *IET Power Electron.* **2012**, *5*, 998–1007. [CrossRef]
16. Jiang, L.; Mi, C.C.; Li, S.; Zhang, M.; Zhang, X.; Yin, C. A Novel Soft-Switching Bidirectional DC-DC Converter with Coupled Inductors. *IEEE Trans. Ind. Appl.* **2013**, *49*, 2730–2740. [CrossRef]
17. Aamir, M.; Mekhilef, S.; Kim, H.J. High-Gain Zero-Voltage Switching Bidirectional Converter with a Reduced Number of Switches. *IEEE Trans. Circuits Syst.* **2015**, *62*, 816–820. [CrossRef]
18. Hwu, K.I.; Jiang, W.Z. Non-Isolated large step-down voltage conversion ratio converter with non-pulsating output current. *Int. J. Circ. Theor. Appl.* **2015**. [CrossRef]
19. Mohammadi, M.R.; Farzanehfard, H. A New Family of Zero-Voltage-Transition Nonisolated Bidirectional Converters with Simple Auxiliary Circuit. *IEEE Trans. Ind. Electron.* **2016**, *63*, 1519–1527. [CrossRef]
20. Lee, K.J.; Park, B.G.; Kim, R.Y.; Hyun, D.S. Nonisolated ZVT Two-Inductor Boost Converter With a Single Resonant Inductor for High Step-Up Applications. *IEEE Trans. Power Electron.* **2012**, *27*, 1966–1973. [CrossRef]
21. Baek, J.B.; Choi, W.I.; Cho, B.H. Digital Adaptive Frequency Modulation for Bidirectional DC-DC Converter. *IEEE Trans. Ind. Electron.* **2013**, *60*, 5167–5176. [CrossRef]
22. Xue, L.K.; Wang, P.; Wang, Y.F.; Bei, T.Z.; Yan, H.Y. A Four-Phase High Voltage Conversion Ratio Bidirectional DC-DC Converter for Battery Applications. *Energies* **2015**, *8*, 6399–6426. [CrossRef]
23. Lai, C.M.; Lin, Y.C.; Lee, D. Study and Implementation of a Two-Phase Interleaved Bidirectional DC/DC Converter for Vehicle and DC-Microgrid Systems. *Energies* **2015**, *8*, 9969–9991. [CrossRef]
24. Gleissner, M.; Bakran, M.M. Design and Control of Fault-Tolerant Nonisolated Multiphase Multilevel DC-DC Converters for Automotive Power Systems. *IEEE Trans. Ind. Appl.* **2016**, *52*, 1785–1795.
25. Lin, C.C.; Yang, L.S.; Wu, G.W. Study of a non-isolated bidirectional DC-DC converter. *IET Power Electron.* **2013**, *6*, 30–37. [CrossRef]
26. Ardi, H.; Ahrabi, R.R.; Ravadanegh, S.N. Non-Isolated bidirectional DC-DC converter analysis and implementation. *IET Power Electron.* **2014**, *7*, 3033–3044. [CrossRef]
27. Serna-Garces, S.I.; Montoya, D.G.; Ramos-Paja, C.A. Sliding-Mode Control of a Charger/Discharger DC/DC Converter for DC-Bus Regulation in Renewable Power Systems. *Energies* **2016**, *9*, 1–27. [CrossRef]
28. Konjedic, T.; Korosec, L.; Truntic, M.; Restrepo, C.; Rodic, M.; Milanovic, M. DCM-Based Zero-Voltage Switching Control of a Bidirectional DC-DC Converter With Variable Switching Frequency. *IEEE Trans. Power Electron.* **2016**, *31*, 3273–3288. [CrossRef]

29. Zhao, B.; Song, Q.; Liu, W.; Sun, Y. Overview of Dual-Active-Bridge Isolated Bidirectional DC–DC Converter for High-Frequency-Link Power-Conversion System. *IEEE Trans. Power Electron.* **2014**, *29*, 4091–4106. [CrossRef]
30. Waffler, S.; Kolar, J.W. A Novel Low-Loss Modulation Strategy for High-Power Bidirectional Buck + Boost Converters. *IEEE Trans. Power Electron.* **2009**, *24*, 1589–1599. [CrossRef]
31. Chiu, H.J.; Lo, Y.K.; Kuo, S.W.; Cheng, S.J.; Lin, F.T. Design and implementation of a high-efficiency bidirectional DC-DC Converter for DC micro-grid system applications. *Int. J. Circ. Theor. Appl.* **2014**, *42*, 1139–1153. [CrossRef]
32. Onar, O.C.; Kobayashi, J.; Khaligh, A. A Fully Directional Universal Power Electronic Interface for EV, HEV, and PHEV Applications. *IEEE Trans. Power Electron.* **2013**, *28*, 5489–5498. [CrossRef]
33. Chen, B.Y.; Lai, Y.S. Switching Control Technique of Phase-Shift-Controlled Full-Bridge Converter to Improve Efficiency Under Light-Load and Standby Conditions Without Additional Auxiliary Components. *IEEE Trans. Power Electron.* **2010**, *25*, 1001–1012. [CrossRef]
34. Lo, Y.K.; Lin, C.Y.; Hsieh, M.T.; Lin, C.Y. Switching Control Technique of Phase-Shift-Controlled Full-Bridge Converter to Improve Efficiency Under Light-Load and Standby Conditions Without Additional Auxiliary Components. *IEEE Trans. Ind. Electron.* **2011**, *58*, 2572–2575. [CrossRef]
35. Kim, J.H.; Kim, C.E.; Kim, J.K.; Lee, J.B.; Moon, G.W. Analysis on Load-Adaptive Phase-Shift Control for High Efficiency Full-Bridge LLC Resonant Converter Under Light-Load Conditions. *IEEE Trans. Power Electron.* **2016**, *31*, 4942–4955.

© 2016 by the authors; licensee MDPI, Basel, Switzerland. This article is an open access article distributed under the terms and conditions of the Creative Commons Attribution (CC-BY) license (http://creativecommons.org/licenses/by/4.0/).